

Influence of Lithium Insertion on the Electronic Transport in Electroactive MoO₃ Nanobelts and Classical Powders: Morphological and Particle Size Effects

S. Berthumeyrie,[†] J.-C. Badot,^{*,‡} J.-P. Pereira-Ramos,[‡] O. Dubrunfaut,[§] S. Bach,[‡] and Ph. Vermaut^{||}

Laboratoire de Chimie de la Matière Condensée de Paris, CNRS UMR 7574, ENSCP, Chimie ParisTech, 11 rue Pierre et Marie Curie, 75231 Paris Cedex 05, France, Institut de Chimie et des Matériaux Paris-Est-Equipe GESMAT-CNRS UMR 7182, 2-8 rue Henri Dunant, 94320 Thiais, France, Département Matériaux, Université Evry Val d'Essonne, Bd. F. Mitterrand 91025 Evry Cedex, France, Laboratoire de Génie Electrique de Paris, CNRS UMR 8507, SUPELEC, UPMC Université Paris 06, Université Paris-Sud, 11 rue Joliot-Curie, Plateau de Moulon, 91192 Gif-sur-Yvette Cedex, France, and Laboratoire de Physico-Chimie des Surfaces, CNRS UMR 7045, ENSCP, Chimie ParisTech, 11 rue Pierre et Marie Curie, 75231 Paris Cedex 05, France

Received: July 22, 2010; Revised Manuscript Received: October 7, 2010

Studying the electronic transport in Li_xMoO₃ powders is of the utmost interest due to the strong influence of the grain size and morphology on their electrochemical cycling properties. An original straightforward synthesis method permitted the obtaining of nanobelts of α -MoO₃ with a slightly better reversibility of Li insertion–deinsertion and a higher efficiency of the lithium insertion process. The broad-band dielectric spectroscopy technique from 40 to 10¹⁰ Hz was applied to Li_xMoO₃ micronic powder and nanobelts. Dielectric relaxations were found, attributed to polarons and bipolarons motions. The role of the morphology and size effect has been investigated by comparing the electron transport properties of micronic powder and nanobelts. Particle size effect is evidenced giving rise to different thermal behaviors between the two types of powders. This work opens up new prospects for a more fundamental understanding of the electronic transport in relation to the electrochemical properties of α -MoO₃.

1. Introduction

Cathode reaction in lithium batteries consists of insertion/deinsertion of Li⁺ ions within a host material during discharge/charge, respectively. Well-known host lattices are, for example, vanadium oxides, various allotropic MnO₂ phases, LiCoO₂, LiMn₂O₄, and LiFePO₄.¹ Many other materials were studied, among them α -MoO₃. Due to its layer structure particularly favorable to lithium insertion, it is indeed one of the first material studied as a cathode for lithium batteries,² and it remains a promising material as its theoretical capacity is about 280 mAh/g (1.5 Li/Mo) for an average potential of 2 V leading to a reversible specific energy of 560 Wh/kg, i.e., comparable to that of V₂O₅. Lithium ions can intercalate the host lattice of α -MoO₃, and Li_xMoO₃ compounds are thus obtained.³ Lithium ions are compensated by excess electrons, reducing Mo⁶⁺ into Mo⁵⁺ (and then Mo⁴⁺) and contributing to the electronic conductivity of Li_xMoO₃.

The knowledge of electronic and ionic transports is required to better understand electrochemical behaviors. Drift mobilities of electrons and ions take part in charge–discharge mechanisms. Nevertheless, the scientific literature is rather scarce on the study of the electronic conductivity of the electrode materials versus their electrochemical behavior. Note that the electrode materials

are especially electronic conductors with negligible ionic conduction. Dc conductivity of α -MoO₃ has been previously investigated for single crystals, powders, and thin films. Conductivity of single crystal⁴ was measured perpendicular to molybdenum trioxide sheets with a value of about 10^{−10} S·cm^{−1} and that of pressed or sintered classical powders between 10^{−10} and 10^{−3} S·cm^{−1}.^{5–7} Differences in stoichiometry and in sintering processes can lead to such differences in conductivity. Conductivity of aggregated powder of nanobelts was estimated at 10^{−5} S·cm^{−1}.⁸ More recently, dc electrical measurements of individual nanobelts⁹ have determined dc conductivity equal to 10^{−4} S·cm^{−1} along MoO₆ zigzag chains. In previous papers, thin films conductivity was measured in the range 10^{−10}–10^{−8} S·cm^{−1}.¹⁰ In some cases, the authors showed that the conductivity of Li_xMoO₃ compounds is high ($\sim 10^{-2}$ S·cm^{−1} for $x = 0.3$) with small activation energy or a quasi-metallic behavior.⁵ Optical measurements on thin films of Li_xMoO₃ were determined over the photon energy range from 0.4 to 4.2 eV and revealed absorption peaks due to the presence of small polarons for $x < 0.7$.¹¹ Moreover, it has been shown that the ionic conductivity (σ_i) in Li_xMoO₃ compounds is negligible compared to the electronic conductivity (σ_e), since $\sigma_e/\sigma_i \approx 10^{-3}$.⁵ Nevertheless, the study of electronic transport properties presents some difficulties because Li_xMoO₃ is in the form of a powder or nanobelts. So, the conductivity measurements by usual dc techniques cannot provide any information on the grain electrical transport properties owing to the existence of local charge motions and of microstructures and/or nanostructures.^{12–16} On the other hand, broad-band dielectric spectroscopy (BDS) techniques are powerful tools for the electrical characterization of powdered materials from macroscopic to

* To whom correspondence should be addressed. E-mail: jc-badot@chimie-paristech.fr.

[†] Laboratoire de Chimie de la Matière Condensée de Paris, CNRS UMR 7574.

[‡] Institut de Chimie et des Matériaux Paris-Est-Equipe GESMAT-CNRS UMR 7182 and Département Matériaux, Université Evry Val d'Essonne.

[§] Laboratoire de Génie Electrique de Paris, CNRS UMR 8507.

^{||} Laboratoire de Physico-Chimie des Surfaces, CNRS UMR 704.

local properties. BDS probes the interaction of a material with a time-dependent electric field. The resulting electrical response is due to charge density fluctuations and thus described by the time-dependent current or dipole correlation function. In the frequency domain, these fluctuations are either expressed by the frequency-dependent complex permittivity ε , conductivity σ , or resistivity ρ . In this way, the relation between the frequency-dependent permittivity $\varepsilon(\omega)$ and conductivity $\sigma(\omega)$ is given by

$$\sigma(\omega) = \rho(\omega)^{-1} = i\omega\varepsilon_0\varepsilon(\omega) \quad (1)$$

where ε_0 is the vacuum permittivity ($\varepsilon_0 = 8.84 \times 10^{-12} \text{ F} \cdot \text{m}^{-1}$). The time scale (or relaxation time) of the fluctuations depends on the scale at which they occur. In electronic conductors, different electrical relaxations generally result from their architecture (microstructure, nanostructure, and crystalline structure). Several polarization mechanisms at different scales with distinct characteristic frequencies can be separated and treated individually.¹⁶ When the frequency increases (or time decreases), different kinds of polarizations appear in the following order: (a) interfacial polarization due to the existence of aggregates (consisting of particles) and particle (grain or nanobelt) boundaries giving rise to dielectric relaxations in the low-frequency domain; (b) polarization due to local charge motions (e.g., small polarons hopping in oxides^{12–20}) giving rise to dielectric relaxations in radiofrequency and microwave frequency domains. Other possible mechanisms include the appearance of polarizations at interphases (e.g., nonpercolated conducting phase in insulating medium) and at interfaces between the sample and the metallic device used in electrical measurements. This later phenomenon occurs generally at lower frequencies than those of the interfacial polarizations within the sample.^{12–18}

In the present paper, we report the first detailed study concerning the influence of lithium insertion on the electronic transport in electroactive MoO_3 nanobelts and classical powders. The electrical properties were recorded between 40 and 10^{10} Hz on Li_xMoO_3 classical powder (hereafter called CP) and nanobelts (hereafter called NB) within the temperature range 200–300 K. The influence of morphology and particle size effects will also be discussed with respect to the lithium insertion and the structure in order to understand the electronic transport in Li_xMoO_3 .

2. Experimental Section

2.1. Synthesis. Classical powder (CP) of MoO_3 is a commercial powder (PROLABO). One of the most known nanoscale structures of $\alpha\text{-MoO}_3$ is nanobelts^{9,21,22} whose synthesis can be made chemically using, for example, acidification of molybdate solution.^{9,21} We manage to find a way to synthesize nanobelts of $\alpha\text{-MoO}_3$ NB at atmospheric pressure. Aqueous sodium molybdate solution (1 M) is passed through a cation-exchange resin. Then, concentrated nitric acid is added to the resulting blue solution. Finally, precipitation occurs during evaporation of solvent at 100 °C. Precipitate is washed with distilled water and dried at 110 °C. This synthesis also provides the lowest minimal temperature necessary to obtain $\alpha\text{-MoO}_3$ nanobelts mentioned in the literature.

The electrochemically lithiated samples contain percolated carbon black and graphite, both with a higher electronic conductivity than that of Li_xMoO_3 . As the electrons will thus prefer to move through the carbon network, it will not be

possible to measure the intrinsic electrical properties of Li_xMoO_3 . It is thus necessary to insert lithium ions chemically by using *n*-butyllithium, as previously described in the literature.² The chemical insertion of lithium ions is made within an Ar-filled glovebox. $\alpha\text{-MoO}_3$ CP and NB dispersed in *n*-hexane and appropriate amounts of a solution of 1.6 M *n*-butyllithium in hexane are added under stirring to reach a given stoichiometry Li_xMoO_3 . Powder is then filtered and rinsed with *n*-hexane. The true stoichiometry of thus lithiated samples is controlled by ICP-OES.

2.2. Structure and Morphology. The XRD diagrams have been recorded on an INEL diffractometer. A large multichannel detector detects diffracted X-rays with a 2θ angle from 0 to 105°. Scanning electron microscopy (SEM) pictures were obtained on a LEO 1530 microscope, classical transmission electron microscopy (TEM) images on a JEOL 2000FX, and high-resolution transmission electron microscopy (HRTEM) images on a JEOL 2010 F microscope.

2.3. Electrochemical Characterizations. Two electrode type Swage-Lock cells are used. The anode is made with a lithium metal pellet. The electrolyte used is 1 M LiPF_6 in EC/DEC 50:50. The cathode is formulated by mixing manually active material, acetylene black, graphite, and PTFE with the following weight proportions, respectively: 80:7.5:7.5:5. Finally, approximately 10 mg of this mixture is put on a spherical piece of stainless steel grid with a diameter of 12.7 mm to be pressed against at a pressure of 10 T for 10 min. The cell is built in an Ar-filled glovebox. Galvanostatic cycling is made at a rate of C/20 (1 mole of lithium ions per mole of molybdenum oxide is inserted/desinserted in 20 h).

2.4. Broad-band Dielectric Spectroscopy. Complex resistivity and permittivity spectra of the microparticles (CP) (PROLABO) and the nanobelts (NB) were recorded over a broad frequency range of 40– 10^{10} Hz, using simultaneously an impedance analyzer (Agilent 4294 from 40 to 1.1×10^8 Hz) and a network analyzer (HP 8510 from 4.5×10^7 to 10^{10} Hz). The experimental device consists of a coaxial cell (APC7 standard) in which the cylindrically shaped sample with silver-plated front faces fills the gap between the inner conductor and a short circuit. The sample CP has the same diameter (3 mm) as the inner conductor (Figure 1a), while the sample NB has the same diameter (7 mm) as the outer conductor of the coaxial cell (Figure 1b).^{12–17,23} Both samples have a thickness of about 1 mm. After a relevant calibration of the analyzers, the complex (relative) permittivity $\varepsilon(\omega) = \varepsilon'(\omega) - i\varepsilon''(\omega)$ of the sample is computed from its reflection coefficient and its admittance. Complete dielectric spectra were made from about 400 measurements with an accuracy of approximately 3–5% in the experimental frequency range. The knowledge of the complex permittivity enables the calculation of the complex resistivity $\rho = \rho' - i\rho'' = (i\omega\varepsilon_0\varepsilon)^{-1}$ (ε_0 being the vacuum permittivity) and conductivity $\sigma = \rho^{-1}$. The samples are compacted powders at 1 GPa, and the measurements were made in the temperature range 200–300 K under dry N_2 flux.

As the nanobelts have a preferential orientation perpendicular to the sample axis, an anisotropy study has been made on the same sample NB. The experimental device (Figure 1c) consists of a coaxial cell^{12–18} loaded to the two ports (1 and 2) of the network analyzer (Agilent PNA E8364B from 10^7 to 10^{10} Hz).²⁴ The samples NB having uniaxial anisotropy fill the gap between the two inner conductors connected to ports 1 and 2. This device permits the simultaneous measurement of the reflection and transmission coefficients, and thus the components ε_{\perp} (i.e., perpendicular to sample axis) and ε_{\parallel} (i.e., parallel to sample

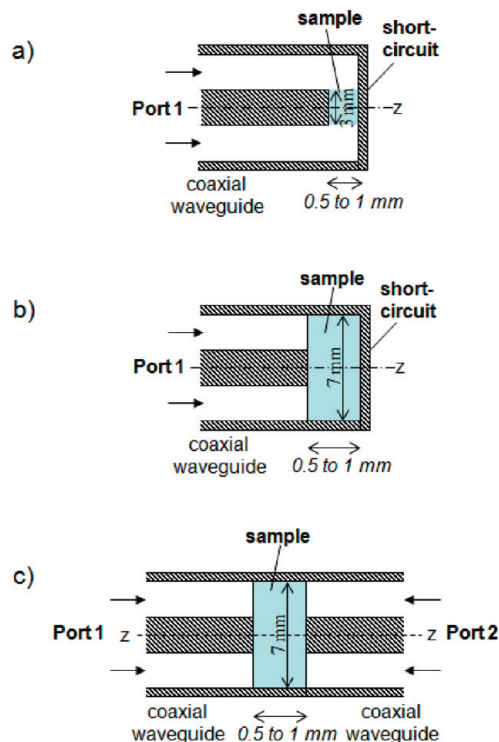


Figure 1. (a) Coaxial cell used to make temperature-dependent measurements of ϵ' and σ vs frequency for Li_xMoO_3 CP; (b) coaxial cell used to make temperature-dependent measurements of ϵ' and σ vs frequency for Li_xMoO_3 NB; (c) coaxial cell used to study the permittivity tensor of $\text{Li}_{0.28}\text{MoO}_3$ NB only at room temperature.

axis) of the permittivity (uniaxial) tensor. Note that measurements vs temperature are not currently possible with such a device.

3. Results and Discussion

3.1. Structure and Morphology of $\alpha\text{-MoO}_3$ Classical Powder and Nanobelts. SEM pictures taken on a LEO 1530SEM of CP and NB are reported in Figures 2a and b, respectively. Figure 2a shows that CP consists mainly of large particles (grains) in the form of platelets with average sizes of $1\ \mu\text{m}$ thick \times $10\ \mu\text{m}$ wide \times $25\ \mu\text{m}$ long. Nanobelts in NB have average sizes of about $30\ \text{nm}$ thick \times $150\ \text{nm}$ wide \times $10\ 000\ \text{nm}$ long (Figure 2b). In both cases, aggregates of platelets or nanobelts are observed.

In Figure 3a, both CP and NB are assigned to be the orthorhombic phase $\alpha\text{-MoO}_3$ (JCPDF No. 05-0508). Peaks belonging to this phase are marked with an asterisk in the whole publication. $\alpha\text{-MoO}_3$ crystallizes in the $Pnma$ space group. The crystallographic structure of this oxide²⁵ is schematized in Figure 3b. Distorted octahedral MoO_6 are linked together using edges on the c -axis in order to make a zigzag chain. Along the a -axis, chains are linked together using vertices. This assembly of chains makes a sheet of $\alpha\text{-MoO}_3$. Sheets are linked together along the b -axis owing to van der Waals forces. Cell parameters have values close to that given in JCPDF 05-0508: $a = 3.98\ \text{\AA}$, $b = 13.85\ \text{\AA}$, $c = 3.69\ \text{\AA}$, and $a = 3.96\ \text{\AA}$, $b = 13.87\ \text{\AA}$, $c = 3.70\ \text{\AA}$ for CP and NB, respectively. In order to determine the coherence length d of nanobelts in the $(0k0)$ direction, the Debye–Scherrer formula is used

$$d = kd_{0k0} = \frac{k\lambda}{\cos(\theta)\sqrt{IW^2 - IW_{\text{ref}}^2}} = \frac{kn\lambda}{\cos(\theta)\sqrt{\text{fwhm}^2 - \text{fwhm}_{\text{ref}}^2}} \quad (2)$$

with θ the diffraction angle of the $(0k0)$ diffraction peak, k the second Miller index of the $(0k0)$ diffraction peak, and λ the X-ray wavelength ($\lambda_{\text{CuK}\alpha} = 1.54\ \text{\AA}$). To qualify the $(0k0)$ peak shape, integral widths (IW) and full widths at half-maximum (fwhm) are used. IW and fwhm refer to studied material, whereas IW_{ref} and fwhm_{ref} refer to a reference sample with large particles or grains, i.e., CP in our case. n is the ratio of fwhm to IW. As Lorentzian profiles are considered here, $n = 0.89$. Owing to the expression 2 used for $(0k0)$ peaks, crystallite size along the b -axis in $\alpha\text{-MoO}_3$ NB is calculated to be around $30\ \text{nm}$, which corresponds to the thickness of nanobelts as is shown in the SEM picture (Figure 2b). TEM observations confirm that the nanobelts are single crystals. A high-resolution image of the nanobelts (Figure 4a) with its Fourier transform depicted in Figure 4b shows that the main crystal growth direction is along the c -axis. This latter fact is in agreement with the literature.⁹

3.2. Electrochemical Characterization. The first galvanostatic discharge–charge profiles of both CP and NB are reported in Figures 5a and b, respectively. The CP profile corresponds to what is described in the literature for $\alpha\text{-MoO}_3$.²⁶ During the first discharge, working potential decreases abruptly to a well-defined plateau located at $2.7\ \text{V}$ and is assigned to a two-phase domain,²⁷ between $\alpha\text{-MoO}_3$ and a new phase (thereafter called α') with the approximate stoichiometry $\text{Li}_{0.25}\text{MoO}_3$. Then,

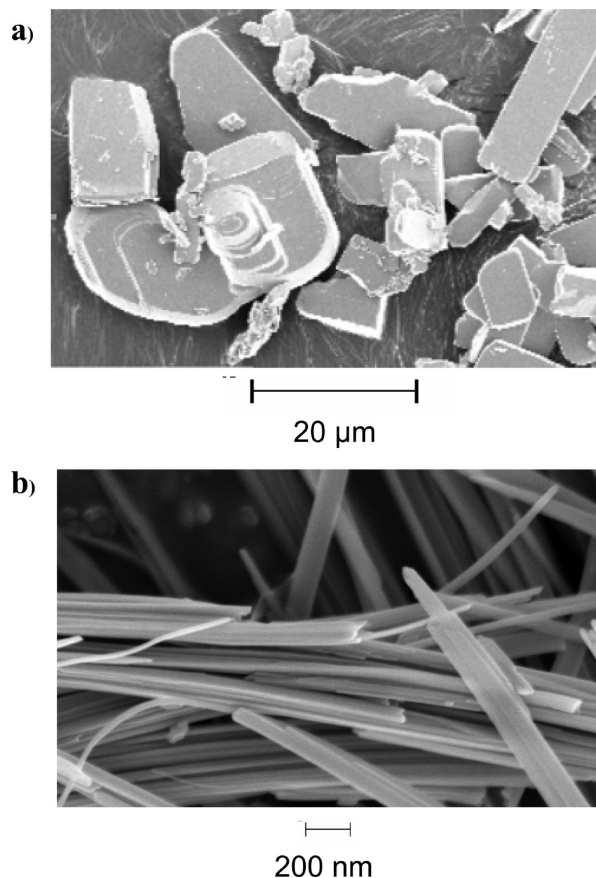


Figure 2. SEM picture of $\alpha\text{-MoO}_3$: (a) classical powder (CP) and (b) nanobelts (NB).

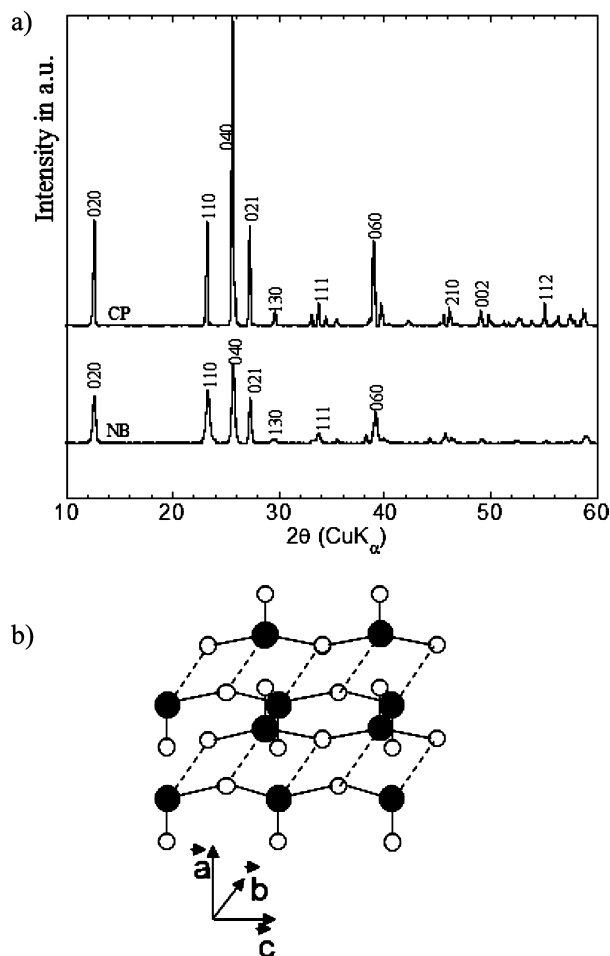


Figure 3. (a) XRD diagrams of a MoO_3 CP and NB ($\text{CuK}\alpha$, $\lambda = 1.54$ Å); (b) schematic representation of the local structure of a MoO_3 sheet.

working potential slowly drops to a “quasi-plateau” at around 2.3 V. Structural evolution in this domain is described in the literature as a solid solution of lithium ions within the α' phase.²⁷ First charge up to 4 V is not a quantitative process since the final composition is around $\text{Li}_{0.25}\text{MoO}_3$. The NB profile shows a higher Li uptake during the first discharge (1.7 for NB vs 1.5 for CP) and slightly higher first charge efficiency than CP (85% for NB vs 81% for CP). Moreover, a solid solution behavior of NB could be suggested for $0 < x < 0.1$ as the potential slowly drops to the biphasic region whereas a biphasic region ($\alpha + \alpha'$) is reported in the case of CP since the first instants of reduction.²⁸

3.3. Crystallographic Structure of Li_xMoO_3 Phases Chemically Synthesized. XRD diagrams of Li_xMoO_3 compounds from classical powder are comparable to those already published²⁷ and depicted in Figure 6a. Peaks belonging to α - MoO_3 are marked with an asterisk. The rapid emergence of a new series of peaks (position in 2θ : 11.4°, 22.8°, 38.4°) for $\text{Li}_{0.1}\text{MoO}_3$ CP is attributed to formation of the α' phase. Presence of both α and α' phases is so clearly shown in its XRD diffraction pattern (Figure 6a) and is linked with the existence of the voltage plateau observed at 2.7 V visible in Figures 3a and b. Sample $\text{Li}_{0.31}\text{MoO}_3$ CP also contains both phases with a very low content of α phase, while $\text{Li}_{0.45}\text{MoO}_3$ CP is only constituted of α' phase. To explain the structure of the α' phase, we have used a model²⁹ in which was suggested the same space group as for α - MoO_3 . Differences between α and α' phases are thus only lying on differences in values of cell parameters. The b parameter of the α' structure ($b = 16$ Å) is higher than that of α - MoO_3 ($b = 13.8$ Å). This

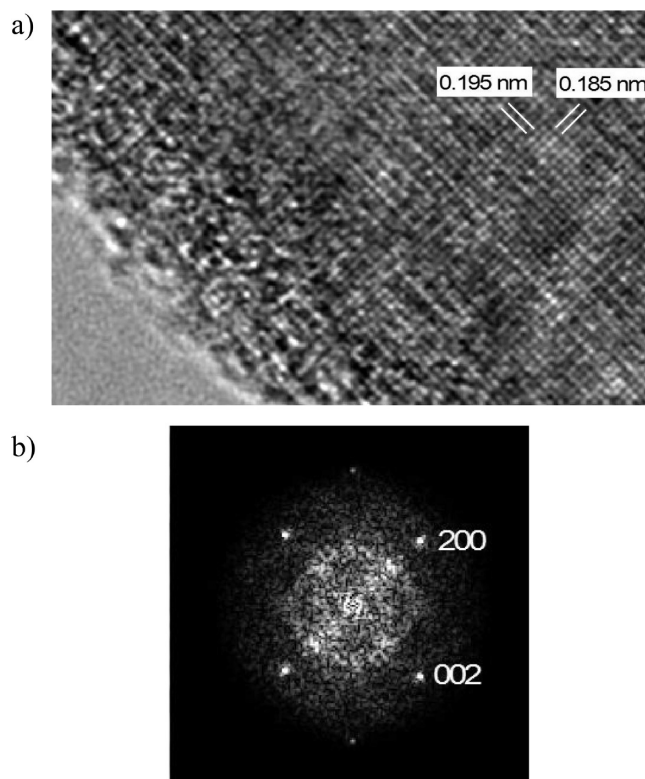


Figure 4. (a) High-resolution TEM pictures of a nanobelt in the ac -plane and (b) corresponding 2D Fourier transform.

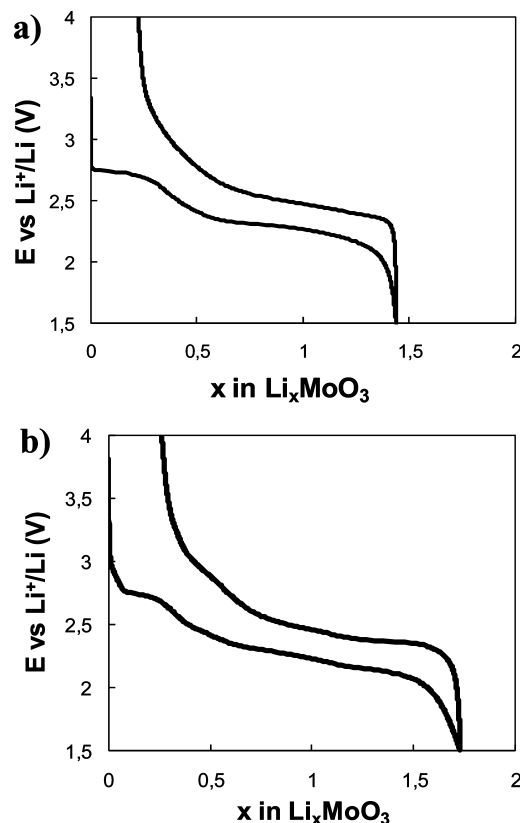


Figure 5. First galvanostatic discharge and charge profile at C/20 rate for α - MoO_3 (a) classical powder (CP) and (b) nanobelts (NB).

increase has been interpreted as a result of lithium insertion within or between sheets. The c parameter is almost constant on the whole domain. As c is related to strong links in the structure, indeed, links of MoO_6 octahedra by edges, this fact

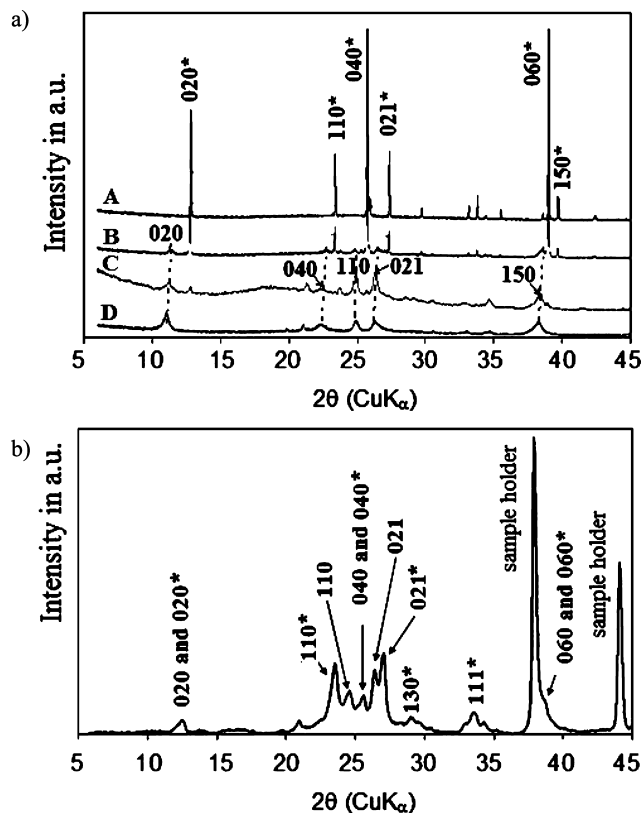


Figure 6. XRD diagrams ($\text{CuK}\alpha$, $\lambda = 1.54 \text{ \AA}$) of Li_xMoO_3 compounds obtained chemically using *n*-butyllithium in *n*-hexane. (a) Classical powder (CP) (A, $x = 0.01$; B, $x = 0.11$; C, $x = 0.31$; D, $x = 0.45$) (* = α phase). (b) Nanobelts (NB) ($x = 0.28$) (* = α_1 phase).

could be understandable. The a parameter of the α' phase is lower than that of α - MoO_3 (3.65 vs 3.98 \AA). As far as we know, no interpretation of this data has been already given in the literature. Here, we suggest it could be due to insertion of lithium ions within sheets and more precisely between MoO_6 zigzag chains.

Considering $\text{Li}_{0.28}\text{MoO}_3$ NB α - MoO_3 powder, two phases related to the α phase are evidenced in Figure 6b: (i) α_1 phase ($a = 3.9 \text{ \AA}$, $b = 14 \text{ \AA}$, $c = 3.72 \text{ \AA}$) and (ii) α_2 phase ($a = 3.73 \text{ \AA}$, $b = 14 \text{ \AA}$, $c = 3.84 \text{ \AA}$). Cell parameters of α_1 are not far from that of α - MoO_3 , while cell parameters of α_2 are more different. So, we suggest that the lithium content in the α_2 phase is higher than in the α_1 phase. As lithium ions come from the surface of nanobelts, α_1 would be located on the nanobelt core while α_2 would be at the surface. As parameter b in both phases is not far from that of α - MoO_3 , it tends to show that lithium ions are located mostly within the sheets. To have an idea of the relative proportion of the lithium rich phase compared with the lithium poor phase, we could compare heights of XRD peaks. This method makes us think the relative proportion of the lithium poor phase is higher in $\text{Li}_{0.28}\text{MoO}_3$ NB compared with $\text{Li}_{0.31}\text{MoO}_3$ CP. It would mean that a transition to the lithium rich phase occurs at higher lithium content in the case of NB compared with CP. This hypothesis is consistent with the literature.³⁰ The authors explain that in nanoparticles structural strain is better accommodated compared with large particles because more defects could be stored at the surface of particles. As a consequence, lithium solubility in a given phase is higher in nanoparticles, and, consequently, emergence of a rich lithium phase occurs at higher lithium content.

3.4. Electronic Transport Properties. The electrical measurements were made on chemically lithiated compounds. The

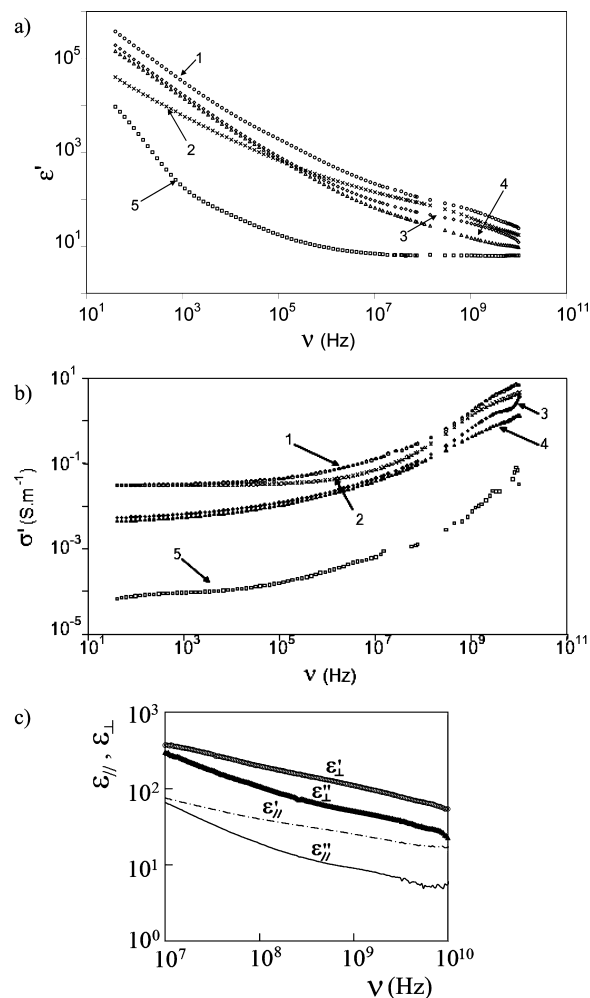


Figure 7. Real parts of (a) the permittivity ϵ' and (b) the conductivity σ' vs frequency for different lithium contents x in MoO_3 classical powder (CP) (1, $x = 0.45$; 2, $x = 0.31$; 4, $x = 0.11$; 5, $x = 0.01$) and nanobelts (NB) (3, $x = 0.28$) at 300 K. (c) Real (ϵ'_{\perp} , ϵ'_{\parallel}) and imaginary (ϵ''_{\perp} , ϵ''_{\parallel}) parts of the components ϵ_{\perp} and ϵ_{\parallel} of the complex permittivity tensor for $\text{Li}_{0.28}\text{MoO}_3$ NB vs frequency at 300 K.

frequency dependences of the real parts of the permittivity (ϵ') and the conductivity (σ') for classical powder (CP) and nanobelts (NB) are shown in Figures 7a and b at 300 K. All dielectric spectra have similar shapes whatever the temperature of the different samples. The real part of the permittivity ϵ' vs frequency decreases by about 4 orders of magnitude from 40 to 10^{10} Hz. For frequency below 10^3 Hz, the values of ϵ' are between 10^4 and 10^5 for lithiated compounds, which indicate a strong capacitive effect. On the other hand, the conductivity vs frequency varies by about 4–5 orders of magnitude from 40 to 10^{10} Hz. However, since the nanobelts have a preferential orientation perpendicular to the sample axis, an anisotropy study has been only made on $\text{Li}_{0.28}\text{MoO}_3$ NB at room temperature (Figure 7c).²⁴ It was thus possible to determine simultaneously the real (ϵ'_{\perp} , ϵ'_{\parallel}) and imaginary (ϵ''_{\perp} , ϵ''_{\parallel}) parts of the components ϵ_{\perp} (i.e., perpendicular to sample axis) and ϵ_{\parallel} (i.e., parallel to sample axis) of the permittivity tensor. Note that the permittivity and the conductivity of the nanobelts measured by the device of Figure 1b are combinations of the components parallel (ϵ'_{\parallel} and σ_{\parallel}) and perpendicular (ϵ'_{\perp} and σ_{\perp}) to the sample axis, respectively. As the relaxations are not clearly evidenced in all the dielectric spectra, we will use the Nyquist representation in order to get easily their decomposition. Since all the polarizations within the samples are additive owing to their

vectorial character, their contributions (relaxations) can be thus evidenced by a decomposition procedure of the different Nyquist plots representing the imaginary part vs real part of the complex variables: permittivity (ϵ'' vs ϵ'), resistivity (ρ'' vs ρ'), and conductivity (σ'' vs σ'). This procedure recorded by homemade software is obtained by successive subtractions of the different contributions from low to microwave frequencies. Dielectric relaxations are currently described by the complex Cole–Cole function

$$\epsilon = \epsilon_H + \frac{\epsilon_L - \epsilon_H}{1 + (i\omega\tau_\epsilon)^{1-\alpha}} \quad (3)$$

where ϵ_H and ϵ_L represent the high- and low-frequency limits of the permittivity of each contribution. τ_ϵ is the mean relaxation time, the relaxation frequency being $\nu_\epsilon = (2\pi\tau_\epsilon)^{-1}$. The relaxation time corresponds to the transit time of the charge carriers at different scales of the material: aggregates, particles (grains, nanobelts), and interatomic distances. The fitting parameter α , which ranges between 0 and 1, is the degree of deviation from the ideal Debye response with $\alpha = 0$. The Cole–Cole function is thus the result of a continuous distribution $G_\epsilon(\tau)$ of the relaxation times, which has a maximum at $\tau = \tau_\epsilon$ and becomes broader for increasing values of the α parameter.³¹ Moreover, the complex resistivity is given by a similar relaxation function

$$\rho = \rho_H + \frac{\rho_L - \rho_H}{1 + (i\omega\tau_\rho)^{1-\alpha}} \quad (4)$$

with ρ_H and ρ_L , respectively, the high- and low-frequency limits of the resistivity and τ_ρ a mean (resistivity) relaxation time. The existence of contact resistances and capacitances between the grains (crystallites) and between the agglomerates will give rise to dielectric and resistivity relaxations. Here, the Cole–Cole function is due to the existence of a continuous distribution $G_\rho(\tau)$ of the relaxation times as a result of a distribution of contact resistances and capacitances. In practice, complex resistivity plots are useful to determine the grain (crystallite) bulk dc conductivity in powdered compounds. However, they can be also used to obtain the conductivity at different scales of the sample (sample and aggregates conductivities). Complex resistivity plots appear to be complementary to complex permittivity plots in order to establish some correlation between conductivities and dielectric relaxation frequencies. In some cases, complex conductivity plots are more suitable owing to the difficulty in interpreting the corresponding resistivity plots. Furthermore, in order to investigate the correlation between the electric conduction mechanisms and the nature of charge carriers (e.g., small and/or large polarons and bipolarons), the temperature dependences of the conductivity and of the different relaxation frequencies are of crucial interest. Obtained activation energies and frequency prefactors (hereafter called attempt frequencies) give often some leads on the charge carrier behaviors. Afterward, the electrical properties of CP and NB will be studied as a function of lithium insertion. In this way, the influence of the size and the morphology will be started up concerning the permittivities and conductivities of CP and NB.

Figure 8a shows the entire complex resistivity diagram, ρ'' versus ρ' , of $\text{Li}_{0.31}\text{MoO}_3$ CP at 300 K. To provide evidence for the different electrical relaxations, we used a decomposition procedure of the Nyquist plots. The dispersion domain R2 is

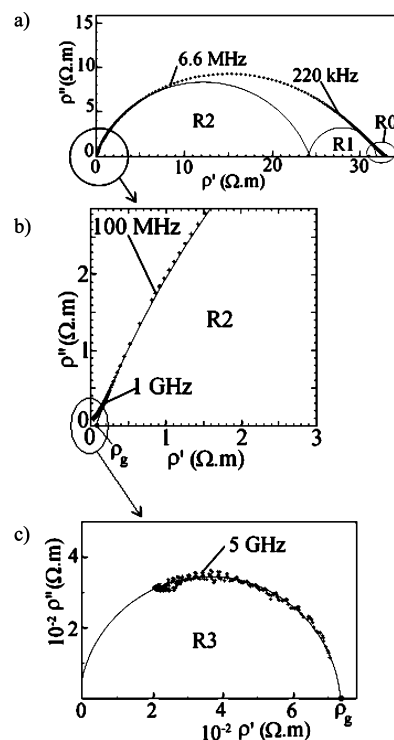


Figure 8. Nyquist plots of the imaginary part $\rho''(\omega)$ vs the real part $\rho'(\omega)$ of the complex resistivity at 300 K for a classical powder (CP) of $\text{Li}_{0.31}\text{MoO}_3$: (a) entire plot from 40 to 10^{10} Hz, evidence of the low-frequency relaxation domains R1 and R2; (b) zoom of the high-frequency part of the plot; (c) high-frequency relaxation domain R3 (grain bulk contribution) upon subtracting the contribution R2. R0 corresponds to very small contribution of interface silver/sample, and ρ_g represents the (effective) resistivity of the grain (crystallite) bulk.

well fitted by a circular arc in the high-frequency part of the plot (Figures 8a and b) and thus described by the complex function of expression 4. R2 crosses the real axis ρ' at ρ_{ag} (Figure 8a) and ρ_g (Figure 8b). After subtraction of the domain R2, the higher frequency contribution R3 is evidenced (Figure 8c) and also fitted by a circular arc described by expression 4. Since R3 crosses the real axis at the origin and at ρ_g , it can be attributed to the grain (platelet or crystallite) bulk contribution. Moreover, the contribution R2 is thus due to contact resistances and capacitances between the grains (crystallites). In the same way, the low-frequency contribution R1 appears and crosses the real axis at ρ_{ag} and ρ_s . R1 (Figure 8a) results from contact resistances and capacitances between the aggregates of grains. A very small contribution R0 appears at lower frequency and would be due to contact resistances and capacitances between the sample and the silver electrodes. Note that ρ_{ag} and ρ_s correspond to the aggregate and the sample resistivities, respectively. All complex resistivity plots of CP are similar whatever the temperature. It is then possible to obtain the grain bulk dc conductivity $\sigma_g = (\rho_g)^{-1}$ at room temperature are listed in Table 1. The conductivities of Li_xMoO_3 NB ($x = 0$ and 0.28) have been obtained in the same way as those of CP. Despite their preferential orientation, Table 1 shows that the conductivity of MoO_3 nanobelts is around 4 orders of magnitude higher than that of MoO_3 platelets. This difference would originate in a higher content of oxygen vacancies contained in nanobelts as a result of the synthesis procedure. Figure 9a shows the variation of the conductivity σ_g of Li_xMoO_3 CP with respect to the lithium content x ($\log \sigma_g$ vs x) at room temperature. For the smaller values of x , the rapid rise of σ_g is typical of percolation behavior

TABLE 1: dc Conductivity (σ) of the Grains at Room Temperature; Activation Energies E_σ , E_p , and E_b of dc Conductivity, Polaron and Bipolaron Motions, Respectively; Relaxation Frequencies (ν) Due to Polaron and Bipolaron Motions at Room Temperature and Their Corresponding Attempt Frequencies (ν_0) for Different Lithium Contents (x)

x	grains			polaron motion			bipolaron motion		
	σ_g at RT ($\text{S}\cdot\text{m}^{-1}$)	E_σ (eV)	ϵ_{hf}	ν_5 at RT (Hz)	E_p (eV)	ν_0 (Hz)	ν_4 at RT (Hz)	E_b (eV)	ν_0 (Hz)
0.00 classical	10^{-8}	—	6.0	—	—	—	—	—	—
0.01 classical	2×10^{-4}	0.54	6.0	1×10^6	0.43	1.6×10^{13}	—	—	—
0.11 classical	0.5	0.07	8.5	2.2×10^9	0.06	2.0×10^{10}	2.5×10^8	0.11	2.0×10^{10}
0.31 classical	12	0.13	14.5	6.5×10^9	0.05	3.6×10^{10}	1.1×10^9	0.11	3.6×10^{10}
0.45 classical	46	0.13	17.0	—	—	—	1.8×10^9	0.10	9.0×10^{10}
0.00 nanobelts	3×10^{-4}	—	6.0	—	—	—	—	—	—
0.28 nanobelts	0.9^a 20^b	0.04	16.0^c 27.0^d	2.2×10^9	0.03	1.0×10^{10}	2.2×10^8	0.06	5.0×10^9

^a This conductivity value measured in reflection is a combination of the conductivities parallel ($\sigma_{\parallel} = 5 \times 10^{-2} \text{ S}\cdot\text{m}^{-1}$ at RT) and perpendicular ($\sigma_{\perp} = 30 \text{ S}\cdot\text{m}^{-1}$ at RT) to the sample axis. ^b This value is the conductivity $\langle\sigma\rangle$ of a hypothetic isotropic medium at RT (see expression 10): system similar to a classical isotropic powder. ^c This permittivity value measured in reflection is a combination of the permittivities parallel ($\epsilon_{\parallel} = 15$) and perpendicular ($\epsilon_{\perp} = 33$) to the sample axis. ^d This value is the permittivity $\langle\epsilon\rangle$ of a hypothetic isotropic medium (see expression 6): system similar to a classical isotropic powder.

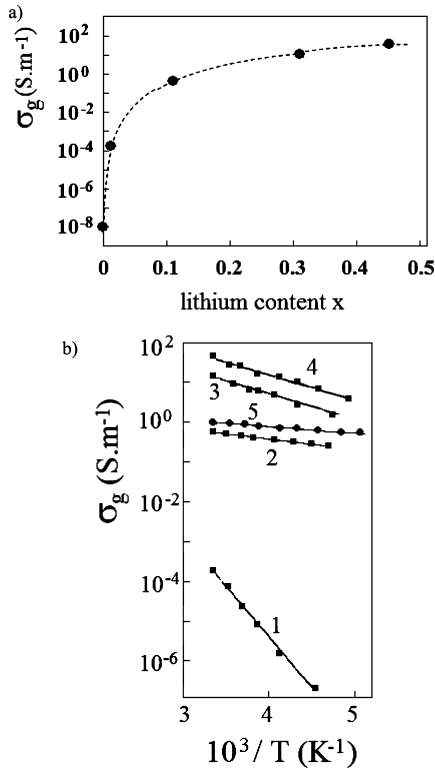


Figure 9. (a) Conductivity $\sigma_g = \rho_g^{-1}$ of Li_xMoO_3 CP as function of lithium content x (i.e., $\log \sigma_g$ vs x), the dotted line being a guide to the eye; (b) direct-current conductivities of the particles (grains and nanobelts) σ_g as functions of inverse temperature T^{-1} (i.e., $\log \sigma_g$ vs T^{-1}) for Li_xMoO_3 CP (1, $x = 0.01$; 2, $x = 0.11$; 3, $x = 0.31$; 4, $x = 0.45$) and Li_xMoO_3 nanobelts (NB) (5, $x = 0.28$).

with a threshold of $x \approx 0.05$. This percolation behavior results from the formation of the continuous conductive phase (above called the α' phase). This result is in good agreement with XRD, which evidenced the appearance of the α' phase for $x \approx 0.03$. Figure 9b shows the resulting temperature dependence of $\sigma_g = (\rho_g)^{-1}$ which have thermally activated behaviors as

$$\sigma_g = \sigma_0 \exp\left(-\frac{E_\sigma}{kT}\right) \quad (5)$$

where k is the Boltzmann constant, σ_0 the conductivity prefactor, and E_σ the activation energy of the conductivity. The values of the different activation energies E_σ are summarized in Table 1.

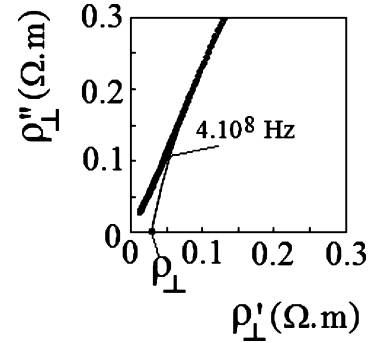


Figure 10. Nyquist plots of the imaginary part $\rho_{\perp}''(\omega)$ vs the real part $\rho_{\perp}'(\omega)$ of the complex resistivity (i.e., perpendicular to the axis of the coaxial line) for $\text{Li}_{0.28}\text{MoO}_3$ nanobelts (NB) at 300 K.

For lower lithium contents ($x = 0.01$), the conductivity activation energy is very high with a value of about 0.51 eV. For higher lithium contents ($x \geq 0.11$), the activation energies are surprisingly low because their values range from 0.07 to 0.13 eV. It results an important change of the conduction mechanism when x varies from 0.01 to 0.11. This phenomenon seems to be correlated to the α' phase formation and will be hereafter interpreted as a result of the complex permittivity plots decomposition. For a quite similar lithium content, the conductivity of $\text{Li}_{0.28}\text{MoO}_3$ NB ($\sigma_g = 0.90 \text{ S}\cdot\text{m}^{-1}$ at 300 K) is lower than that of $\text{Li}_{0.31}\text{MoO}_3$ CP ($\sigma = 12 \text{ S}\cdot\text{m}^{-1}$ at 300 K) but with a lower activation energy $E_s = 0.04$ eV instead of 0.13 eV (Figure 9b and Table 1). Nevertheless, the conductivity of the NB sample is a combination of σ_{\perp} and σ_{\parallel} (see above), while the conductivity of the isotropic CP sample is an average value, i.e., $\sigma_g = \langle\sigma\rangle$. In order to compare precisely NB and CP conductivities, we consider a hypothetical isotropic medium where the mean conductivity is

$$\langle\sigma\rangle = \frac{2\sigma_{\perp}}{3} + \frac{\sigma_{\parallel}}{3} \quad (6)$$

with σ_{\perp} and σ_{\parallel} as defined above. Figure 10 shows the complex resistivity plot which allows determination of σ_{\perp} . Moreover, σ_{\parallel} is obtained in the same way since the corresponding complex resistivity plot is similar to that of Figure 10. From expression 6 and using the experimental values, we obtain $\sigma_{\perp} = 30 \text{ S}\cdot\text{m}^{-1}$ and $\sigma_{\parallel} = 5 \times 10^{-2} \text{ S}\cdot\text{m}^{-1}$ at 300 K. Consequently, an isotropic medium $\text{Li}_{0.28}\text{MoO}_3$ NB would have a mean conductivity $\langle\sigma\rangle \approx 20 \text{ S}\cdot\text{m}^{-1}$ at 300 K (Table 1). The conductivity of $\text{Li}_{0.28}\text{MoO}_3$

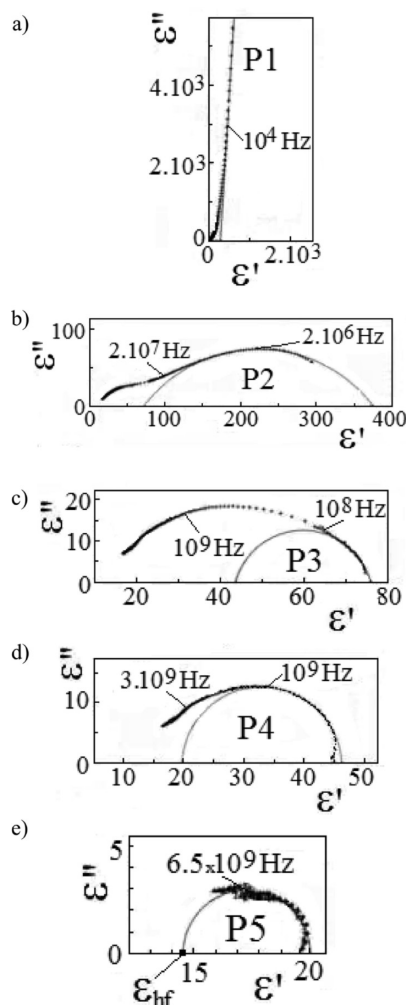


Figure 11. Cole–Cole plots of the imaginary part $\varepsilon''(\omega)$ vs the real part $\varepsilon'(\omega)$ of the complex permittivity at 300 K for a classical powder of $\text{Li}_{0.31}\text{MoO}_3$: (a) entire plot from 40 to 10^{10} Hz: only the low-frequency contribution P0 is visible; (b) plot obtained upon subtracting the domain P0 and evidence of the relaxation domain P1; (c) plot obtained upon subtracting the domain P1 and evidence of the relaxation domain P2; (d) plot obtained upon subtracting the domain P2 and evidence of the relaxation domain P3; (e) plot obtained upon subtracting the domain P3 and evidence of the relaxation domain P4. ε_{hf} corresponds to the (effective) permittivity of lithiated MoO_3 network (i.e., without the contributions of the different relaxations).

NB is intrinsically a little higher than that of $\text{Li}_{0.31}\text{MoO}_3$ CP ($\sigma_g = 12 \text{ S} \cdot \text{m}^{-1}$) at 300 K, but with a lower activation energy. This result is due to different morphologies, sizes, and conduction mechanisms, the surface playing a more important part in the case of the nanobelts.

Figures 11a and 12a show entire Cole–Cole plots, i.e., $\varepsilon''(\omega)$ vs $\varepsilon'(\omega)$, of $\text{Li}_{0.31}\text{MoO}_3$ CP and $\text{Li}_{0.28}\text{MoO}_3$ NB, respectively, from 40 to 10^{10} Hz at 300 K. The first dispersion domains (P1) are fitted between 40 and 10^5 Hz with a good precision by straight lines which correspond to a $\nu^{\alpha-1}$ frequency response of the complex permittivity with exponents α equal to 0.07 and 0.18 for CP and NB, respectively. Furthermore, the real part of the permittivity ε' rises to a high value, around 10^5 at 40 Hz, which indicates high capacitive effects of the sample–metal (silver) junctions. This type of junction is a partially blocking and ohmic contact, giving rise to the existence of a limited charge flow (resistive part) and a polarization (capacitive part) at the junction. The dispersion domains (P1) constitute the high-frequency parts of relaxations (see eq 3) due to junction

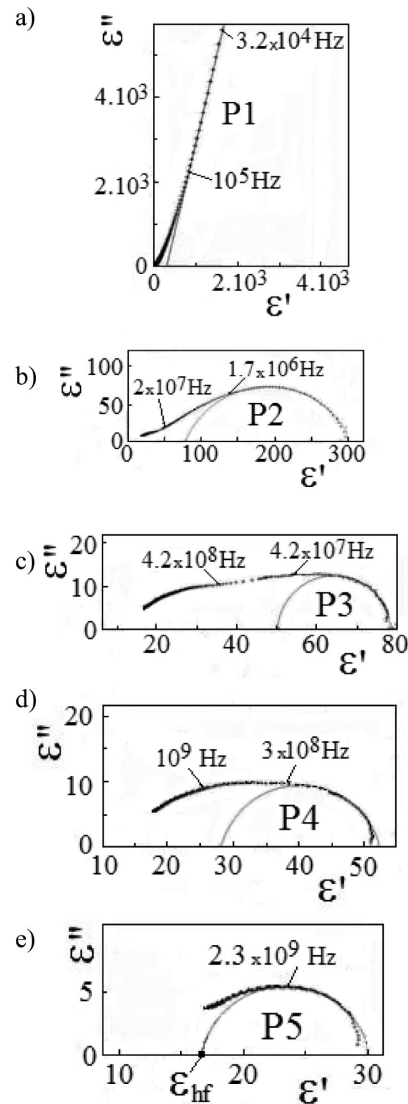


Figure 12. Cole–Cole plots of the imaginary part $\varepsilon''(\omega)$ vs the real part $\varepsilon'(\omega)$ of the complex permittivity at 300 K for nanobelts of $\text{Li}_{0.28}\text{MoO}_3$: (a) entire plot from 40 to 10^{10} Hz: only the low-frequency contribution P0 is visible; (b) plot obtained upon subtracting the domain P0 and evidence of the relaxation domain P1; (c) plot obtained upon subtracting the domain P1 and evidence of the relaxation domain P2; (d) plot obtained upon subtracting the domain P2 and evidence of the relaxation domain P3; (e) plot obtained upon subtracting the domain P3 and evidence of the relaxation domain P4. ε_{hf} corresponds to the (effective) permittivity of lithiated MoO_3 network (i.e., without the contributions of the different relaxations).

polarizations.^{12–16} Upon subtracting these low-frequency contributions, second dispersion domains P2 (Figures 11b and 12b) are evidenced and well fitted by circular arcs corresponding to dielectric relaxations described by Cole–Cole functions (see eq 3). The relaxation frequencies ν_2 are 1.5×10^6 and 7×10^5 Hz for $\text{Li}_{0.31}\text{MoO}_3$ CP and $\text{Li}_{0.28}\text{MoO}_3$ NB, respectively, at room temperature. By the same procedure, the higher frequency relaxation domains P3 (Figures 11c and 12c), P4 (Figures 11d and 12d), and P5 (Figures 11e and 12e) are unambiguously defined by circular arcs and thus described by Cole–Cole functions (see eq 1). For the dispersion domain P3, the relaxation frequencies ν_3 are 8×10^7 and 2×10^7 Hz for $\text{Li}_{0.31}\text{MoO}_3$ CP and $\text{Li}_{0.28}\text{MoO}_3$ NB, respectively, at room temperature. The higher frequency domains P4 and P5 have frequencies $\nu_4 = 1.1 \times 10^9$ and 2.2×10^8 Hz and $\nu_5 = 6.5 \times 10^9$ and 2.2×10^9 Hz for $\text{Li}_{0.31}\text{MoO}_3$ CP and $\text{Li}_{0.28}\text{MoO}_3$ NB, respectively, at room

temperature (Table 1). In the case of the compounds $\text{Li}_{0.01}\text{MoO}_3$ CP and $\text{Li}_{0.45}\text{MoO}_3$ CP, the complex permittivity plots have four components, i.e., only one high-frequency relaxation. Nevertheless, the basic compounds MoO_3 CP and NB have not been well-defined Cole–Cole plots owing to their low permittivity (for CP and NB) and conductivity (for CP) within the wide frequency range. Differences in conductivities at room temperature for these two samples have to be noticed, as for NB, conductivity is 10^4 times higher than CP. This fact for nonlithiated compounds could be a consequence of higher nonstoichiometry for the NB sample. It is likely to be a consequence of synthesis. Although some difference in oxidation state provides huge differences in conductivity, it does not affect permittivity.

Apart from the sample/silver interface, the polarization sources are the aggregates (containing particles), the particles (grains or nanobelts), and the charge carrier's motions in CP and NB. Since the aggregates are less conductive and have larger sizes, the relaxation of their polarization will occur at lower frequency than that of the particles, as previously discussed.¹⁶ In this way, the relaxation domains P2 and P3 can be attributed to the polarizations of the aggregates and the particles, respectively. Concerning the aggregates, the values of the characteristic frequencies ν_2 are dependent on the lithium content x and thus on the electronic conductivity: ν_2 increases from 20 to 1.5×10^6 Hz (at RT) when x rises from 0.01 to 0.45. The characteristic frequencies ν_3 of the particles' polarization vary in the same way, since ν_3 increases from 4×10^4 to 8×10^7 Hz (at RT) with increasing lithium content x . Otherwise, the higher frequency relaxations P4 and P5 can thus be associated to local motions of (electronic) charge carriers (e.g., polarons and bipolarons). The values of their relaxation frequencies ν_4 and ν_5 (at room temperature) are listed in Table 1. Figures 13a and b show the resulting temperature dependence of ν_4 and ν_5 which have thermally activated behaviors as

$$\nu = \nu_0 \exp\left(-\frac{E}{kT}\right) \quad (7)$$

where ν_0 is an attempt frequency and E the activation energy.

For the α -phase $\text{Li}_{0.01}\text{MoO}_3$ CP, the slow relaxation frequency (i.e., 1×10^6 Hz at 300 K) or low mobility (Table 1) is due to strong electron localization and thus associated with small polaron hopping from a molybdenum site to another one along chains parallel to the c -axis. This motion is defined by high activation energy $E_p = 0.43$ eV and attempt frequency $\nu_0 = 1.6 \times 10^{13}$ Hz (Table 1). This activation energy corresponds to a small polaron binding energy $2E_p = 0.86$ eV, which is in good agreement with that determined by previous optical absorption measurements.¹¹ Moreover, the attempt frequency is near the phonon frequency values obtained by the same author.¹¹ As a result, the small polaron hopping is adiabatic²⁰ and the corresponding conductivity is thus expressible in the form

$$\sigma_g = \frac{C}{T} \exp\left(-\frac{E_\sigma}{kT}\right) \quad (7a)$$

where C is the conductivity prefactor (Figure 14). Note that both expressions 5 and 7a fit the temperature dependence of the conductivity owing to a limited temperature range. The obtained activation energy is slightly higher with a value of about 0.54 eV instead of 0.51 eV. We observe that E_p is lower

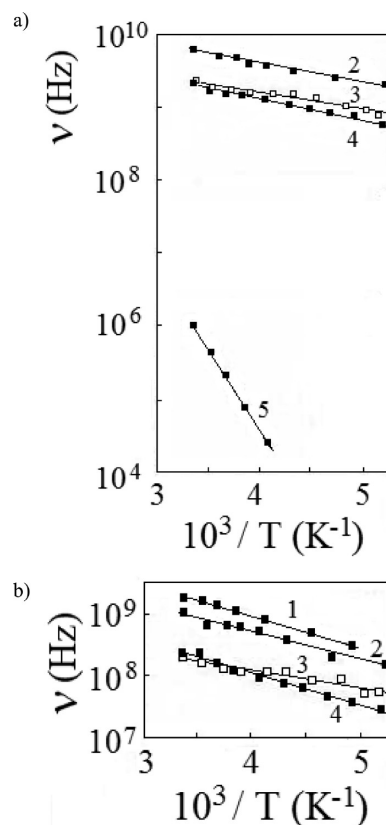


Figure 13. (a) Relaxation frequencies of polaron motion as function of inverse temperature T^{-1} ($\log \nu$ vs T^{-1}) in Li_xMoO_3 classical powder (CP) (2, $x = 0.31$; 4, $x = 0.11$; 5, $x = 0.01$) and nanobelts (3, $x = 0.28$). (b) Relaxation frequencies of bipolaron motion as function of inverse temperature T^{-1} ($\log \nu$ vs T^{-1}) in CP (1, $x = 0.45$; 2, $x = 0.31$; 4, $x = 0.11$) and NB ($x = 0.28$).

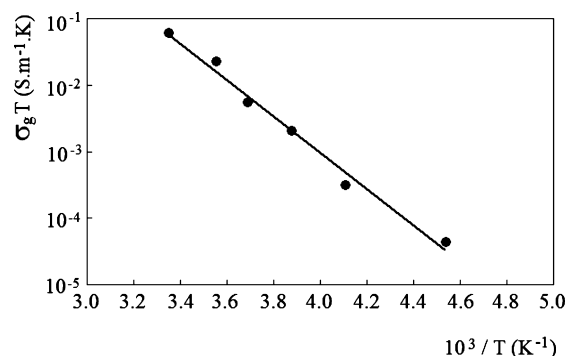


Figure 14. Inverse temperature dependence of the conductivity of $\text{Li}_{0.01}\text{MoO}_3$ CP in the case of an adiabatic hopping, i.e., $\log \sigma_g T$ vs T^{-1} .

than the activation energy of the conductivity E_σ (0.54 eV), the difference being $E = E_\sigma - E_p = 0.11$ eV. In this way, the conduction mechanism in $\text{Li}_{0.01}\text{MoO}_3$ CP is predominantly due to hopping of the charge carriers (small polarons) thermally excited from donors (lithium ions) and can be therefore described by a two-step process:

(i) The first one consists of extracting the electron from the electrostatic field of the lithium ion^{32–34} with a probability proportional to $\exp(-E/kT)$, where $2E = 2(E_\sigma - E_p) = 0.22$ eV is the Coulomb interaction between lithium and polaron.

(ii) The second is a small polaron hopping transfer to a neighboring site^{32–34} with an activation energy $E_p = 0.43$ eV.

For $x \geq 0.11$, the relaxation frequencies ν_4 and ν_5 assigned to local motions have respectively lower activation energies E_4

and E_5 than that in $\text{Li}_{0.01}\text{MoO}_3$, since $0.08 < E_4 < 0.11$ eV and $0.04 < E_5 < 0.05$ eV (Table 1). Since the bipolaron drift mobility is lower, the relaxations 4 and 5 can be attributed to (intersite) bipolarons and to polarons, respectively. Indeed, the increase of the electronic population makes easier the formation of polaron pairs on two neighboring molybdenum sites (i.e., $\text{Mo}^{5+}-\text{Mo}^{5+}$ pairs), because the bipolaron has a lower mobility than that of the isolated polarons.³⁵ A bipolaron forms when the indirect attraction between charge carriers, which results from the electron–lattice interaction, exceeds the Coulomb repulsion between them. The singlet ground state of the bipolaron has a spin $S = 0$. Since the bipolaron charge is $(-2e)$ and $E_4 = 2E_5$, the activation energies E_4 and E_5 correspond to half of the Coulomb interactions lithium–bipolaron and lithium–polaron, respectively. The conduction mechanism in $\text{Li}_{0.11}\text{MoO}_3$ CP is mainly due to polaron motion because $E_\sigma \approx E_5$ (E_5 being hereafter called E_p , see Table 1) and can be therefore described by the following two-step process:

(i) The first one would consist of extracting an isolated polaron from the electrostatic field of the lithium ion^{32–34} with a probability proportional to $\exp(-E_p/kT)$, where $2E_p = 0.12$ eV is here the Coulomb interaction between lithium and polaron.

(ii) The second would be a polaron tunneling transfer to a neighboring (lithium) trapping center.

In another way, the conduction mechanism in $\text{Li}_{0.31}\text{MoO}_3$ CP is mainly due to bipolaron motion because $E_\sigma \approx E_4 = 2E_5$ (E_5 being hereafter called $E_b = 2E_p$, see Table 1) and will be therefore described by the same type of two-step process as for $\text{Li}_{0.11}\text{MoO}_3$ CP, but with a probability of transfer equal to $\exp(-E_b/kT)$, where $2E_b = 0.22$ eV is the Coulomb interaction between lithium and bipolaron for the first step. In $\text{Li}_{0.45}\text{MoO}_3$ CP, no isolated polaron is present since the relaxation 5 does not appear. The conduction mechanism in this latter compound is completely due to bipolaron motion as for $\text{Li}_{0.31}\text{MoO}_3$ CP. When x varies from 0.01 to 0.11, the activation energy drop for the different electron motions could be attributed to decreases of (a) coupling constants of polaron and bipolaron as a result of the α' phase percolation; (b) Coulomb interaction energy drop. Whatever the x values (between 0 and 0.5), the electronic conductivity is due to transfers of bound small polarons, but with different mechanisms according to α or α' phases. In small-polaron model of Holstein,³⁶ the transition temperature T_t marking the transition between band ($T < T_t$) and hopping ($T > T_t$) regimes lies in the range from 0.25 to 0.50 $h\nu_{\text{ph}}/k$. The hopping conduction dominates in the α phase, whereas the band conduction dominates in the α' phase. This change of the conduction mechanism is correlated to an increase of the transition temperature T_t , when x varies from 0.01 to 0.11. From Holstein theory, the polaron band conduction dominates over hopping conduction as long as the small-polaron bandwidth D is important. This phenomenon would be due to a lower electron–lattice constant in the α' phase. However, Austin and Mott³³ have shown that Coulomb interaction drop with increasing doping is usual in semiconductors. They evidenced such drop for increasing lithium content in NiO and suggested an increase of the permittivity due to the presence of occupied donors, i.e., [lithium ion–electron] dipoles (hereafter called $[\text{Li}^+-e^-]$ dipoles). Note that the increase of the permittivity involves a decrease of the Coulomb interaction between lithium ions and electrons. In this way, Figure 15 shows that the high-frequency permittivity ϵ_{hf} of Li_xMoO_3 CP follows a linear dependence with respect to the lithium content x , that is to say

$$\epsilon_{\text{hf}} = 6 + 25x \quad (8)$$

Expression 8 shows that the permittivity of Li_xMoO_3 is directly proportional to the content x of $[\text{Li}^+-e^-]$ dipoles explaining the drop of the activation energies as previously observed by Austin and Mott.³³ The static permittivity of MoO_3 CP, which is equal to 6, corresponds to lattice (vibrations) and electronic contributions (in the UV–vis frequency range) of the polarizability.³⁷ Nevertheless this value is smaller than that of about 18 measured on polycrystalline MoO_3 .³⁸ This difference is completely due to the sample porosity estimated to be 30% whatever the value of x . We have thus to multiply our experimental permittivity values by 3. General effective medium (GEM) theory,^{12,13,39} describes how to calculate the conductivity and the permittivity of a porous sample, i.e., consisting of conductive and insulating phases. The experimental values of the dc conductivity σ_g and permittivity ϵ_{hf} can be compared to that of a hypothetical compact medium σ_G and ϵ_{HF}

$$\frac{(1-\phi)(1-\epsilon_{\text{hf}}^{1/u})}{\phi_c + (1-\phi_c)\epsilon_{\text{hf}}^{1/u}} + \frac{\phi(\epsilon_{\text{HF}}^{1/u} - \epsilon_{\text{hf}}^{1/u})}{\phi_c\epsilon_{\text{HF}}^{1/u} + (1-\phi_c)\epsilon_{\text{hf}}^{1/u}} = 0 \quad (9)$$

$$\frac{\sigma_g}{\sigma_G} = \left[\frac{\phi - \phi_c}{1 - \phi_c} \right]^u \quad (10)$$

where ϕ is the volume fraction of the conductive phase, ϕ_c is the critical percolation threshold, and u is a critical exponent.^{12,13,39} Unfortunately, it was not possible to have access to a wide range of porosity values to determine exactly both parameters ϕ_c and u . However, it was possible to estimate the order of magnitude of the permittivity and the conductivity knowing parameters of the GEM theory. For 3D systems, ϕ_c is generally between 0.10 and 0.40 and u between 1.65 and 2. Considering the ratio $\epsilon_{\text{HF}}/\epsilon_{\text{hf}} = 3$, the limiting values of u , and the sample porosity $p = (1-\phi)$ at about 30%, we therefore have $0.16 < \phi_c < 0.23$ and $2.3 < (\sigma_G/\sigma_g) < 2.4$. As Li_xMoO_3 phases are 1D conductors (along the c -axis), the conductivity (along the c -axis) will be therefore $3\sigma_G$, i.e., about 7 times the conductivity values indicated in Table 1. As the (intersite) bipolarons are only the charge carriers in monophased $\text{Li}_{0.45}\text{MoO}_3$ CP, it is possible to determine easily their drift mobility

$$\mu_d = \frac{\sigma_c}{ne} \quad (11)$$

from the knowledge of the conductivity σ_c along the c -axis and the number n of individual electronic charges (e) participating in the conduction. Since $n = 2 \times 10^{28} \exp(-0.13/kT)$ (in m^{-3}) (Table 1) and $\sigma_c = 322 \text{ S}\cdot\text{m}^{-1}$ at room temperature, we obtain $\mu_d = 0.32 \text{ cm}^2 \text{ V}^{-1} \text{ s}^{-1}$ at room temperature. This value is high in comparison with the small-polaron mobility ($\mu_d = 10^{-2} \text{ cm}^2 \text{ V}^{-1} \text{ s}^{-1}$) in the hopping regime.⁴⁰ This μ_d value would thus correspond to the small-polaron mobility in the band regime.

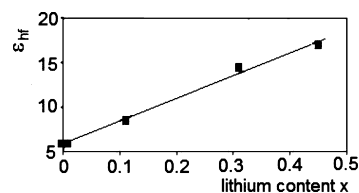


Figure 15. High-frequency permittivity ϵ_{hf} of the classical powder (CP) as function of the lithium content x .

Contrarily to $\text{Li}_{0.31}\text{MoO}_3$ CP, the conduction mechanism in $\text{Li}_{0.28}\text{MoO}_3$ NB is mainly due to polaron motion because $E_\sigma \approx E_5 = E_p$ (Table 1) and can be therefore described by a two-step process previously described. Characteristics of polaron motions are near that of $\text{Li}_{0.11}\text{MoO}_3$ CP. As lithium solubility is higher in the α phase in the case of nanoparticles compared with micrometric ones, transition to lithium rich phase occurs at higher lithium content. As a consequence, characteristics of $\text{Li}_{0.28}\text{MoO}_3$ NB could be similar to those of the CP sample with lower lithium content. To compare permittivities of $\text{Li}_{0.28}\text{MoO}_3$ NB and $\text{Li}_{0.30}\text{MoO}_3$ CP, it is necessary to take into account the preferential orientation of the nanobelts in $\text{Li}_{0.28}\text{MoO}_3$ NB. As for the conductivity and in order to make a comparison, we consider a hypothetical isotropic medium with mean permittivity

$$\langle \epsilon \rangle = \frac{2\epsilon_{\perp}}{3} + \frac{\epsilon_{\parallel}}{3} \quad (12)$$

where ϵ_{\perp} and ϵ_{\parallel} were defined above. From expression 12 and using the experimental values $\epsilon_{\perp} = 33$ and $\epsilon_{\parallel} = 15$, we obtain $\langle \epsilon \rangle \approx 27$. Consequently, an isotropic medium consisting of nanobelts would have a mean high-frequency permittivity of about 27 at room temperature (Table 1). In this way, the high-frequency permittivity of $\text{Li}_{0.28}\text{MoO}_3$ NB is higher than that of $\text{Li}_{0.31}\text{MoO}_3$ CP (Table 1). Clearly, the presence of more defects in NB cannot explain this difference, because permittivities of the basic compounds NB and CP are the same although NB contains more defects. This result could be due to morphology and size effects on the permittivity, the surface playing the main part in the case of the nanobelts. The region of the material (semiconductor) close to the surface can be depleted of its electrons and is thus positively charged.^{34,41} This non-uniform charge distribution (space-charge) induces an electrostatic field which tends to align the $[\text{Li}^+ - \text{e}^-]$ dipoles in the surroundings of the nanobelts and thus increases the permittivity (polarization) of $\text{Li}_{0.28}\text{MoO}_3$ NB in comparison to that of $\text{Li}_{0.31}\text{MoO}_3$ CP (Table 1). To sum up, permittivity (ϵ_{hf}) of lithiated compounds has a supplementary contribution of the $[\text{Li}^+ - \text{e}^-]$ dipoles in addition to that of lattice and electronic transitions. Moreover, a higher mean permittivity value of $\text{Li}_{0.28}\text{MoO}_3$ NB induces smaller activation energy in the same proportion, owing to the Coulomb interaction.

For $x \geq 0.11$, the attempt frequencies ν_0 would be the characteristic frequencies of the fast $[\text{Li}^+ - \text{e}^-]$ dipoles motions, i.e., electron motions on Mo sites around lithium ions. Their characteristic frequencies ν_0 are in the range $2.0 \times 10^{10} - 9 \times 10^{10}$ Hz for Li_xMoO_3 CP. In the case of $\text{Li}_{0.28}\text{MoO}_3$ NB, $[\text{Li}^+ - \text{e}^-]$ dipoles motions are slowed down ($\nu_0 \approx 1.0 \times 10^{10}$ Hz) under the action of the electrostatic field in the surroundings of the nanobelts.

We may anticipate that lithium ions will tend to segregate on the nanoparticle surface. Consequently, insertion and deinsertion of lithium ions would be faster, since diffusion on the particle surface requires lower energy than that in the particle bulk. This hypothesis agrees with experimental evidence of a better reversibility of Li insertion–deinsertion for the nanobelt powder after several electrochemical cycles. However, further ^7Li NMR measurements on classical particles and nanobelts of Li_xMoO_3 have to be performed to establish more precise information on lithium sites and environment.

3. Conclusion

In this paper are reported the synthesis of nanobelts of $\alpha\text{-MoO}_3$ and the electronic transport properties of Li_xMoO_3

(nanobelts and classical powder) in the temperature range 200–300 K. Nanobelts of $\alpha\text{-MoO}_3$ were obtained by an original route at atmospheric pressure and at lower temperature than in previous papers. X-ray diffraction studies have shown some differences concerning the crystal structure of the micronic powder and the nanobelts. A better reversibility of Li insertion–deinsertion for the nanobelt powder was observed after several electrochemical cycles. The first determination of the electronic conductivity and the permittivity of Li_xMoO_3 (microparticles and nanobelts) over a wide frequency range of $40 - 10^{10}$ Hz is reported with respect to the lithium content, the size, and the morphology. Interpretation of the spectra was made possible through the knowledge of the structures previously studied by X-ray diffraction and electron microscopy. A combination of complex resistivity and permittivity diagrams has allowed the determination of the electrical behavior with the temperature. In summary, different electrical relaxations were shown on Li_xMoO_3 , resulting from the polarizations at the different scales of the samples: (i) polaron and bipolaron motions along chains parallel to the c -axis, (ii) grains (crystallites), and (iii) aggregates of grains. For micronic particles (classical powder), the change from polaronic to bipolaronic conduction has been evidenced with the increase of the lithium content x . On the other hand, this conduction change was not observed in the case of nanobelts owing to morphology and size effects. This phenomenon was attributed to a stronger surface effect for nanobelts giving rise to a different conduction mechanism. Moreover, the influence of the permittivity was reported on its action on the electronic transport in Li_xMoO_3 .

This work opens up new and very exciting prospects for a more fundamental understanding as well as a more rational optimization of the electronic transport in Li_xMoO_3 . It will be pursued by varying the size and the morphology of the powders (e.g., synthesis of particles with smaller sizes) to have a more complete influence on these parameters. In the future, it will be necessary to establish a correlation of electronic conduction with electrochemical behavior of electrodes consisting of MoO_3 .

Acknowledgment. The authors thank the “EADS Foundation” for financial support.

References and Notes

- (1) Whittingham, M. S. *Chem. Rev.* **2004**, *104* (10), 4271.
- (2) Besenhard, J. O.; Heydecke, J.; Fritz, H. P. *Solid State Ionics* **1982**, *6* (3), 215. Besenhard, J. O.; Heydecke, J.; Wudy, E.; Fritz, H. P.; Foag, W. *Solid State Ionics* **1983**, *8* (1), 61.
- (3) Besenhard, J. O.; Schöllhorn, R. *J. Power Sources* **1976–1977**, *1*, 267.
- (4) Pandit, A. K.; Prasad, M.; Ansari, T. H.; Singh, R. A.; Wanklyn, B. M. *Solid State Commun.* **1991**, *80* (2), 125.
- (5) Julien, C.; Nazri, G. A. *Solid State Ionics* **1994**, *68*, 111.
- (6) Honma, K.; Hirota, K.; Yamaguchi, O.; Asai, J.; Makiyama, Y. *Mater. Res. Bull.* **1997**, *32* (1), 1.
- (7) Pokhrel, S.; Nagaraja, K. S. *Phys. Status Solidi A* **2002**, *194* (1), 140.
- (8) Hu, X. K.; Qian, Y. T.; Song, Z. T.; Huang, J. R.; Cao, R.; Xiao, J. Q. *Chem. Mater.* **2008**, *20* (4), 1527.
- (9) Mai, L.; Hu, B.; Chen, W.; Qi, Y.; Lao, C.; Yang, R.; Dai, Y. *Adv. Mater.* **2007**, *19*, 3712.
- (10) Julien, C.; Khelfa, A.; Hussain, O. M.; Nazri, G. A. *J. Cryst. Growth* **1995**, *156*, 235.
- (11) Hussain, Z. *J. Electron. Mater.* **2002**, *31*, 615.
- (12) Ragot, F.; Badot, J. C.; Baffier, N.; Fourier-Lamer, A. *J. Mater. Chem.* **1995**, *5*, 1155.
- (13) Badot, J. C.; Bianchi, V.; Baffier, N.; Belhadj-Tahar, N. E. *J. Phys.: Condens. Matter* **2002**, *14*, 6917.
- (14) Badot, J. C.; Mantoux, A.; Baffier, N.; Dubrunfaut, O.; Lincot, D. *J. Mater. Chem.* **2004**, *14*, 3411.
- (15) Badot, J. C.; Mantoux, A.; Baffier, N.; Dubrunfaut, O.; Lincot, D. *J. Phys. Chem. Solids* **2006**, *67*, 1270.

- (16) Badot, J. C.; Ligneel, E.; Dubrunfaut, O.; Guyomard, D.; Lestriez, B. *Adv. Funct. Mater.* **2009**, *19*, 2749.
- (17) Pecquenard, B.; Badot, J. C.; Baffier, N.; Belhadj-Tahar, N. E. *Phys. Status Solidi A* **1997**, *159*, 469.
- (18) Badot, J. C.; Beluze, L.; Dubrunfaut, O. *J. Phys. Chem. C* **2008**, *112*, 14549.
- (19) Fröhlich, H. *Adv. Phys.* **1954**, *3*, 325. *Arch. Sci.* **1957**, *10*, 5.
- (20) Bosman, A. J.; van Daal, A. J. *Adv. Phys.* **1970**, *19*, 1.
- (21) Hu, X. K.; Ma, D. K.; Xu, L. Q.; Zhu, Y. C.; Qian, Y. T. *Chem. Lett.* **2006**, *35* (8), 962.
- (22) Mizushima, T.; Fukushima, K. Ohkita, H.; Kakuta, N. *Appl. Catal., A: Mater. Sci. Process.* **2006**, *82*, 19. Lou, X. W.; Zeng, H. C. *Chem. Mater.* **2002**, *14*, 4781. Subba Reddy, C. V.; Deng, Z. R.; Zhu, Q. Y.; Dai, Y.; Zhou, J.; Chen, W.; Mho, S.-I. *Appl. Phys. A: Mater. Sci. Process.* **2007**, *89*, 995.
- (23) Colomban, Ph.; Mouchon, E.; Belhadj-Tahar, N. E.; Badot, J. C. *Solid State Ionics* **1992**, *813*, 53–56.
- (24) Belhadj-Tahar, N. E.; Fourier-Lamer, A. *IEEE Trans. MTT* **1991**, *39*, 1718.
- (25) Kihlberg, L. *Ark. Kemi* **1963**, *21*, 357.
- (26) Spahr, M. E.; Novak, P.; Haas, O.; Nesper, R. *J. Power Sources* **1995**, *54*, 346.
- (27) Tsumura, T.; Inagaki, M. *Solid State Ionics* **1997**, *104*, 183.
- (28) Hashem, A. M.; Askar, M. H.; Winter, M.; Albering, J. H.; Besenhard, J. O. *Ionics* **2007**, *13*, 3.
- (29) Dickens, P. G. Reynolds, G. J. *Proceedings of Climax Molybdenum, 4th International Conference on Chemistry and Uses of Molybdenum*; Barry, C. H. F., Mitchell, P. C. H., Eds.; Climax Molybdenum Co.: Ann Arbor, MI, 1982; p 35.
- (30) Wagemaker, M.; Borghols, W. J. H.; Mulder, F. M. *J. Am. Chem. Soc.* **2007**, *129*, 1387. Sudant, G.; Baudrin, E.; Larcher, D.; Tarascon, J. M. *J. Mater. Chem.* **2005**, *15*, 1263. Hu, Y. S.; Kienle, L.; Guo, Y. G.; Maier, J. *Adv. Mater.* **2006**, *18*, 1421. Baudrin, E.; Cassaigon, S.; Koelsch, M.; Jolivet, J. P.; Dupont, L.; Tarascon, J. M. *Electrochem. Commun.* **2007**, *9*, 337.
- (31) Böttcher, C. F. J.; Bardewijk, P. In *Theory of electric polarization, 2nd ed., Vol. 2; Dielectrics in time-dependent fields*; Elsevier: Amsterdam, Oxford, 1978.
- (32) Sanchez, C.; Henry, C. M.; Grenet, J. C.; Livage, J. *J. Phys. C: Solid State Phys.* **1982**, *15*, 7133.
- (33) Austin, I. G.; Mott, N. F. *Adv. Phys.* **2001**, *50*, 757.
- (34) Beluze, L.; Badot, J. C.; Weil, R.; Lucas, V. *J. Phys. Chem. B* **2006**, *110*, 7304.
- (35) Alexandrov, A. S.; Mott, N. F. In *Polarons and Bipolarons*; World Scientific: Singapore, 1995.
- (36) Holstein, T. *Ann. Phys. NY* **1959**, *8*, 343.
- (37) Shannon, R. D. *J. Appl. Phys.* **1993**, *73*, 348.
- (38) Deb, S. K.; Chopoorian, J. A. *J. Appl. Phys.* **1966**, *37*, 4818.
- (39) McLachlan, D. S. *Solid State Commun.* **1987**, *60*, 821.
- (40) Goodenough, J. B. In *Progress in Solid State Chemistry*; Reiss, H., Ed.; Pergamon: Oxford, 1971; Vol. 5, p 145, Chapter 4.
- (41) Bube, R. H. In *Electrons in Solids*; Academic Press: New York, 1981.

JP106837G